

**Estimators of Bolometric Luminosity and Black Hole Mass
with Mid-infrared Continuum Luminosities for Dust-obscured Quasars:
Prevalence of Dust-obscured SDSS Quasars***

DOHYEONG KIM,¹ MYUNGSHIN IM,^{2,3} MINJIN KIM,⁴ YONGJUNG KIM,⁴ SUHYUN SHIN,^{2,3} HYUNJIN SHIM,⁵ AND
HYUNMI SONG⁶

¹*Department of Earth Sciences, Pusan National University, Busan 46241, Republic of Korea*

²*Astronomy Program, Dept. of Physics & Astronomy, Seoul National University, Seoul 08826, Republic of Korea*

³*SNU Astronomy Research Center (SNU ARC), Astronomy Program, Dept. of Physics & Astronomy, Seoul National University, Seoul 08826, Republic of Korea*

⁴*Department of Astronomy and Atmospheric Sciences, College of Natural Sciences, Kyungpook National University, Daegu 41566, Republic of Korea*

⁵*Department of Earth Science Education, Kyungpook National University, 80 Daehak-ro, Buk-gu, Daegu 41566, Republic of Korea*

⁶*Department of Astronomy and Space Science, Chungnam National University, 99 Daehak-ro, Yuseong-gu, Daejeon 34134, Republic of Korea*

ABSTRACT

We present bolometric luminosity (L_{bol}) and black hole (BH) mass (M_{BH}) estimators based on mid-infrared (MIR) continuum luminosity (hereafter, L_{MIR}) that are measured from infrared (IR) photometric data. The L_{MIR} -based estimators are relatively immune from dust extinction effects, hence they can be used for dust-obscured quasars. To derive the L_{bol} and M_{BH} estimators, we use unobscured quasars selected from the Sloan Digital Sky Survey (SDSS) quasar catalog, which have wide ranges of L_{bol} ($10^{44.62}$ – $10^{46.16}$ erg s⁻¹) and M_{BH} ($10^{7.14}$ – $10^{9.69}$ M_{\odot}). We find empirical relations between (i) continuum luminosity at 5100 Å (hereafter, L_{5100}) and L_{MIR} ; (ii) L_{bol} and L_{MIR} . Using these relations, we derive the L_{MIR} -based L_{bol} and M_{BH} estimators. We find that our estimators allow the determination of L_{bol} and M_{BH} at an accuracy of ~ 0.2 dex against the fiducial estimates based on the optical properties of the unobscured quasars. We apply the L_{MIR} -based estimators to SDSS quasars at $z \lesssim 0.5$ including obscured ones. The ratios of L_{bol} from the L_{MIR} -based estimators to those from the optical luminosity-based estimators become larger with the amount of the dust extinction, and a non-negligible fraction ($\sim 15\%$) of the SDSS quasars exhibits ratios greater than 1.5. This result suggests that dust extinction can significantly affect physical parameter derivations even for SDSS quasars, and that dust extinction needs to be carefully taken into account when deriving quasar properties.

Keywords: (galaxies:) quasars: supermassive black holes — (galaxies:) quasars: general — (galaxies:) quasars: emission lines — infrared: galaxies — galaxies: evolution

1. INTRODUCTION

In recent years, supermassive black holes (SMBHs) have been found at the centers of spheroidal galaxies. In many observational studies, the masses of SMBHs are well known to have correlations with the properties of their host galaxies, e.g., luminosities (Graham 2007; Bentz et al. 2009; Gültekin et al. 2009; Bennert et al. 2010; Greene et al. 2010), stellar velocity dispersions (σ_* ; Ferrarese & Merritt 2000; Gebhardt et al.

2000; Tremaine et al. 2002; Gültekin et al. 2009; Woo et al. 2010), and Sérsic or concentration indices (Graham et al. 2001; Graham & Driver 2007) of their spheroids. These empirical relationships imply the coevolution of SMBHs and galaxies (for review, see Kormendy & Ho 2013).

Although the detailed physical mechanisms of the coevolution are still unknown, SMBHs have been considered to play an important role in galaxy growth. These SMBHs are believed to grow by accreting gas (Lynden-Bell 1969) in an active phase, i.e., the period of

* dh.dr2kim@gmail.com (DK); myungshin.im@gmail.com (MI)

active galactic nuclei (AGNs), and quasars refer to the ultraluminous active phase.

Although quasars emit their enormous energy in all wavelengths (i.e., gamma-ray to radio), X-ray, ultraviolet (UV), optical, and radio observations have been mainly used to discover quasars. Based on these surveys, previous studies (Grazian et al. 2000; Becker et al. 2001; Anderson et al. 2003; Croom et al. 2004; Risaliti & Elvis 2005; Schneider et al. 2005; Véron-Cetty & Véron 2006; Pâris et al. 2014; Lyke et al. 2020) have found ~ 1 million quasars to date.

However, there is a possibility that the previous quasar surveys can miss a large number ($< 50\%$) of red-colored quasars (Comastri et al. 2001; Tozzi et al. 2006; Polletta et al. 2008). Here, red quasars refer to quasars with red continua from the optical to near-IR (NIR; e.g., $r' - K > 5$ mag; Urrutia et al. 2009), and red quasars can include both type 1, type 2, and extremely red quasars (e.g., Hamann et al. 2017). Many hot dust-obscured galaxies (Eisenhardt et al. 2012; Wu et al. 2012) also fall into this category. Their red colors are suspected to come from the extinction effects of the intervening material in their host galaxies (Webster et al. 1995; Cutri et al. 2001). These red quasars have been considered a different population from normal quasars (i.e., unobscured quasars).

Several simulation studies (e.g., Menci et al. 2004; Hopkins et al. 2005, 2006, 2008) predicted red quasars can be an intermediate population between gas-rich merger-driven star-forming galaxies, often seen as ultraluminous infrared galaxies (Sanders et al. 1988; Sanders & Mirabel 1996), and unobscured quasars after sweeping away the dust and gas by the quasar-driven outflow. From this point of view, red quasars are young and dust-obscured quasars, in which dust obscuration is due to the remaining gas and dust in their host galaxies.

Several pieces of observational evidence have supported this scenario. For example, red quasars have (i) dusty red colors (Kim & Im 2018), (ii) high Eddington ratios ($\lambda_{\text{Edd}} = L_{\text{bol}}/L_{\text{Edd}}$, where L_{bol} and L_{Edd} are the bolometric and Eddington luminosities, respectively; Urrutia et al. 2012; Kim et al. 2015a; Kim & Im 2018; Kim et al. 2018, 2022), (iii) high fractions of merging features (Urrutia et al. 2008; Glikman et al. 2015), (iv) prospective merging SMBH candidates (Kim et al. 2020), and (v) enhanced star-formation activities (Georgakakis et al. 2009), as expected in the merger-driven galaxy evolution scenario.

However, the interpretation of red quasars is still controversial since several studies have provided different explanations for red quasars. For example,

Wilkes et al. (2002) and Rose et al. (2013) explained that the red colors of red quasars come from a moderate viewing angle of dust torus in the unification model (Antonucci 1993). Moreover, other studies (Puchnarewicz & Mason 1998; Whiting et al. 2001; Maddox & Hewett 2006; Young et al. 2008; Rose et al. 2013; Ruiz et al. 2014) suggested that red quasars have intrinsically red continua without any dust extinction. Also, an unusual hot dust covering factor (Rose 2014) and a synchrotron emission peak at NIR wavelength (Whiting et al. 2001) were proposed as alternative explanations for the red colors of red quasars.

To investigate whether red quasars are dust-obscured quasars as expected in the merger-driven galaxy evolution scenario, λ_{Edd} is a key property. However, the λ_{Edd} values of only < 100 red quasars have been measured (e.g., Urrutia et al. 2012; Kim et al. 2015a; Kim & Im 2018; Kim et al. 2018, 2022), and the limited sample size can cause the controversy in the interpretation of red quasars.

To obtain λ_{Edd} , two fundamental physical quantities, bolometric luminosities and BH masses, should be measured. The bolometric luminosity is the total radiative energy in all wavelengths. Measuring the bolometric luminosity accurately is an arduous task since it needs full wavelength observation at least from $1 \mu\text{m}$ to 10 keV or 100 keV (e.g., Krawczyk et al. 2013). However, the bolometric luminosities have empirical relations with various monochromatic continuum luminosities at UV and optical (e.g., 1450 \AA and 5100 \AA ; Elvis et al. 1994; Kaspi et al. 2000; Richards et al. 2006; Runnoe et al. 2012), and these relationships have been widely used.

The BH masses can be measured by using velocity widths of broad lines and sizes of broad-line regions (BLRs). The velocity width can be parameterized by full width at half maximum (FWHM). The size of BLR can be determined from a reverberation mapping technique (Peterson et al. 2004), but the reverberation mapping method is time-consuming. Therefore, the BLR size has been mainly estimated from a single-epoch spectrum based on empirical relations between the BLR sizes and UV or optical continuum luminosities (e.g., Kaspi et al. 2005).

However, despite that the FWHM values even measured in UV and optical cannot be affected by the dust extinction effects, the UV and optical continuum fluxes are easily affected by the extinction in dust-obscured systems. Of course there is the rare possibility that the FWHM could change if the BLR is partially obscured by dust, but Kim et al. (2018) showed that the FWHM values of $\text{H}\beta$, $\text{H}\alpha$, $\text{P}\beta$, and $\text{P}\alpha$ lines of red quasars are not sufficiently different. On the contrary, their Balmer

line luminosities are significantly suppressed compared to their Paschen line luminosities. For example, if a red quasar is obscured by a color excess of $E(B-V) = 1$ mag (Glikman et al. 2007; Kim et al. 2015a, 2018), its continuum fluxes at 5100 \AA and 1450 \AA are suppressed by factors of 22.5 and 2100, respectively, which is calculated by performing FM_UNRED code (Fitzpatrick 1999) with an assumption of $R_V = 3.1$ (e.g., Weingartner & Draine 2001).

For red quasars, therefore, the two fundamental quantities (L_{bol} and M_{BH}) estimated from the UV and optical indicators can be easily affected by the dust extinction. To alleviate the dust extinction effects, the Paschen- and Brackett-line-based M_{BH} (Kim et al. 2010, 2015a,b) and L_{bol} (Kim et al. 2022) estimators were derived. However, the Paschen and Brackett line properties can be achieved through IR spectroscopic observations that have been rarely performed.

In contrast, IR photometry has been extensively obtained by several large area surveys, such as the Two Micron All Sky Survey (2MASS; Cutri et al. 2003) and Wide-field Infrared Explorer (WISE; Wright et al. 2010). The IR photometry represents the IR continuum shape dominated by dust component radiations (e.g., Kim et al. 2015b). The AGN dust emission arises from a dust torus that is believed to surround the accretion disk and SMBH in the Unification model (Antonucci 1993). The dust component can be broadly divided into two subcomponents depending on their temperatures, and the two subcomponents are hot ($> 1000 \text{ K}$; e.g., Barvainis 1987) and warm ($\sim 200 \text{ K}$; e.g., Netzer et al. 2007) dust components. The hot dust component radiation peaks at $\sim 2\text{--}3 \mu\text{m}$, which is known to dominate mid-IR (MIR) quasar continuum (e.g., Kim et al. 2015b).

MIR continuum luminosities have been known to be used as the L_{bol} and M_{BH} estimators. This approach is supported by several observational studies that (i) the hot dust luminosities and the dust torus sizes have empirical correlations with the bolometric luminosities (Kim et al. 2015b; Suganuma et al. 2006); (ii) the bolometric luminosities are correlated with the BLR sizes (Kaspi et al. 2000).

The L_{MIR} -based estimators can be used for dust-obscured systems. The MIR continuum luminosities are relatively immune from the dust extinction. For example, for the case of a quasar at $z = 0$ of which $E(B-V) = 1$ mag, its fluxes at the $W1$ - ($3.4 \mu\text{m}$) and $W2$ - ($4.6 \mu\text{m}$) bands only decrease by factors of 1.20 and 1.14, respectively. Note that this effect is dependent on redshift, but the $W1$ - and $W2$ -band fluxes of low- z ($\lesssim 0.5$) quasars are still relatively immune from dust extinction. If we assume a quasar at $z = 0.5$ and with

$E(B-V) = 1$, the $W1$ - and $W2$ -band wavelengths in the rest-frame are 2.27 and $3.07 \mu\text{m}$, respectively, and their continuum fluxes also only decrease by factors of 1.35 and 1.23, respectively.

Furthermore, the MIR continuum luminosities can be used as common indicators for both unobscured and red quasars. Kim & Im (2018) showed that ratios of the hot dust luminosities to the bolometric luminosities for the two kinds of quasars are not significantly different. Although Ichikawa et al. (2019) reported that the hot dust luminosity ratios of the two types of quasars can be different, there have been several results that the different ratios can be introduced from a selection bias (Elitzur 2012; Lanz et al. 2019).

In this paper, we find empirical relationships between the bolometric luminosities and MIR continuum luminosities. Moreover, we derive BH mass estimators based on a combination of the optical-line FWHM values and the MIR continuum luminosities. Since (i) the MIR continuum luminosities can be measured from the all-sky IR photometric data (2MASS and WISE) and (ii) optical spectra are more accessible than IR spectra, these L_{MIR} -based estimators can be extensively used to investigate the nature of red quasars. The L_{MIR} -based M_{BH} estimators are derived using the FWHM of the broad-line component of $\text{H}\beta$ line, and therefore, it can only be applied to type 1 red quasars. Hereafter, red quasars refer to type 1 red quasars. Moreover, we examine the importance of the dust extinction correction by applying the L_{MIR} -based estimators to a general population of Sloan Digital Sky Survey (SDSS) quasars. We expect these estimators can also be applied to different types of dust-obscured quasars (e.g., intermediate-type and Compton thick quasars), but the M_{BH} estimators would only be feasible when their broad-line component is visible.

Throughout this work, we use a standard Λ CDM model of $H_0 = 70 \text{ km s}^{-1} \text{ Mpc}^{-1}$, $\Omega_m = 0.3$, and $\Omega_\Lambda = 0.7$. This model has been supported by observational studies conducted in recent years (e.g. Im et al. 1997; Planck Collaboration et al. 2016).

2. THE SAMPLE AND DATA

Our sample is drawn from the SDSS Data Release 14 (DR14) quasar catalog (Pâris et al. 2018). The SDSS DR14 quasar catalog contains 526,265 spectroscopically confirmed quasars, and they have a wide redshift range of 0.004–6.97. Moreover, this catalog provides several IR photometric survey data, such as the 2MASS Point Source Catalog (PSC; Cutri et al. 2003) and WISE (Wright et al. 2010; Mainzer et al. 2011) All-WISE Point Source Catalog (Cutri et al. 2021).

Rakshit et al. (2020) measured the spectral properties of the SDSS DR14 quasars by performing multi-component fitting with PyQSOFit code (Guo et al. 2019; Shen et al. 2019). They provide the measured FWHM values of several broad emission lines, such as $H\alpha$, $H\beta$, Mg II, C IV, and $Ly\alpha$. Moreover, the BH masses are also measured based on various FWHM values and continuum luminosities (e.g., Vestergaard & Peterson 2006; Shen et al. 2011), expressed as

$$\log\left(\frac{M_{\text{BH}}}{M_{\odot}}\right) = \alpha + \beta \log\left(\frac{\lambda L_{\lambda}}{10^{44} \text{ erg s}^{-1}}\right) + 2 \log\left(\frac{\text{FWHM}}{1000 \text{ km s}^{-1}}\right). \quad (1)$$

We adopt the optical-line-based FWHM values and BH masses presented in Rakshit et al. (2020). The $\text{FWHM}_{H\beta}$ and $\text{FWHM}_{H\alpha}$ are adopted as the optical broad-line FWHM values. Moreover, the BH masses were measured with the $\text{FWHM}_{H\beta}$ and L5100 by using 0.91 and 0.50 for the α and β values in Equation 1, respectively (Vestergaard & Peterson 2006).

Among the SDSS DR14 quasars, we select the quasars that satisfy the following condition: (1) being detected with good signal-to-noise ratio (S/N), (2) being unobscured, and (3) being brighter than a uniform detection limit. We select quasars that are detected with an $S/N > 3$ in the J , H , K bands (from 2MASS PSC), as well as in $W1$ and $W2$ bands (from *WISE*).

SDSS quasars are known to also include dust-obscured quasars (e.g., Richards et al. 2003), hence we choose unobscured quasars among the SDSS quasars. First, the unobscured quasars are chosen by using broad line Balmer decrement. The $L_{H\alpha}/L_{H\beta}$ values of unobscured quasars have been found to vary from 3.06 (Dong et al. 2008), which is similar to the value of 3.1 predicted by Case B recombination. However, the Balmer decrements are distinct for radio-loud and -quiet quasars. For instance, the $\log\left(\frac{L_{H\alpha}}{L_{H\beta}}\right)$ values were found to be 0.528 ± 0.057 and 0.483 ± 0.046 for radio-loud and -quiet quasars, respectively (Dong et al. 2008), and hence we consider the bimodality of the Balmer decrement to select unobscured quasars. Second, we select the unobscured quasars via spectral energy distribution (SED) fitting. We perform the SED fitting for the SDSS quasars as described in Section 3. The SED fitting yields a color excess, $E(B - V)$, and red quasars have been classified as having high $E(B - V)$ values (e.g., $E(B - V) > 0.1$; Urrutia et al. 2009). In this work, we use the SDSS quasars with Balmer decrement and color excess ranges of (i) $(0.528 - 3 \times 0.057) < \log\left(\frac{L_{H\alpha}}{L_{H\beta}}\right) < (0.483 + 3 \times 0.046)$; and (ii) $E(B - V) < 0.1$ as unobscured

quasars. Note that the Balmer decrement criterion can include some mildly obscured radio-loud quasars. However, we expect that the remaining mildly obscured quasars are ultimately rejected by the $E(B - V) < 0.1$ criterion.

Moreover, we choose the quasars using a uniform detection limit to eliminate the effects from the different detection limits of the SDSS, 2MASS, and *WISE* data. Since the 2MASS data have shallower detection limits (e.g., 14.3 mag at the K_s band) than SDSS and *WISE*, we measure the SDSS and *WISE* magnitude limits that correspond to the detection limit of 2MASS. In order to measure the magnitude limits, we assume a quasar at $z = 0.25$ with K_s -band magnitude of 14.3, and measure its r - and $W2$ -band magnitudes, where we use the AGN template of Richards et al. (2006). The measured r - and $W2$ -band magnitude limits are 17.14 (AB) mag and 11.48 (Vega) mag, respectively. We select the SDSS quasars that are brighter than the magnitude limits of the r , K_s , and $W2$ bands.

We then match these quasars to the quasars in Krawczyk et al. (2013), and adopt the bolometric luminosities. For measuring the bolometric luminosities, the photons from $\sim 1 \mu\text{m}$, excluding IR emissions, to $\sim 10 \text{ keV}$ have been widely used (e.g., Runnoe et al. 2012; Kim et al. 2022). Hence, we adopt the $1 \mu\text{m}$ – 10 keV luminosities measured in Krawczyk et al. (2013) as the bolometric luminosities. Note that several previous studies (e.g., Richards et al. 2006) used different wavelength ranges (e.g., $100 \mu\text{m}$ – 10 keV) for measuring the bolometric luminosities, resulting in discrepancies in the bolometric luminosity measurements, and the discrepancy is shown in Figure 5.

Krawczyk et al. (2013) measured the $1 \mu\text{m}$ – 10 keV luminosities of SDSS DR7 quasars using broadband data from the FUV to the MIR, and compensated for the lack of the X-ray data by applying an $L_{\text{UV}}-L_{\text{X}}$ relation (Steffen et al. 2006). These bolometric luminosity measurements are reliable, and the rms difference in the $1 \mu\text{m}$ – 10 keV luminosities from Krawczyk et al. (2013) and Richards et al. (2006) for 250 overlapped quasars was only 0.07 dex (Kim et al. 2022).

Figures 1 and 2 show the basic properties of the selected 129 SDSS quasars. Our sample is at low redshift ($0.06 < z < 0.42$), but spans over somewhat wide ranges of BH mass ($10^{7.14} M_{\odot} < M_{\text{BH}} < 10^{9.69} M_{\odot}$) and bolometric luminosity ($10^{44.62} \text{ erg s}^{-1} < L_{\text{bol}} < 10^{46.16} \text{ erg s}^{-1}$).

3. SED FITTING FOR CONTINUUM LUMINOSITIES

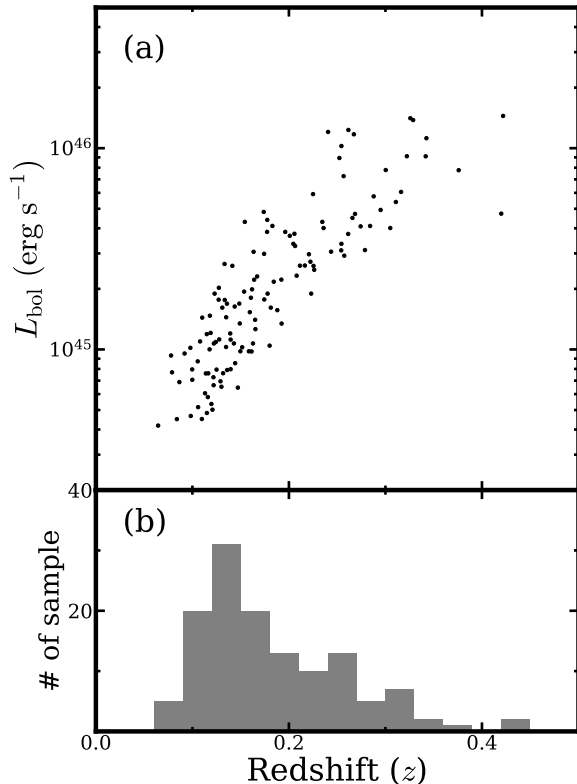


Figure 1. (a): Redshift versus bolometric luminosity. The bolometric luminosities are adopted from [Krawczyk et al. \(2013\)](#). (b): Redshift distribution of our sample.

In order to establish the L_{MIR} -based L_{bol} and M_{BH} estimators, we use the monochromatic continuum luminosities, λL_{λ} , at $3.4 \mu\text{m}$ and $4.6 \mu\text{m}$ (hereafter $L_{3.4}$ and $L_{4.6}$, respectively) in the rest-frame, which correspond to the $W1$ - and $W2$ -band wavelengths of the *WISE* photometric system. However, the host galaxy contamination is non-negligible in MIR luminosity, and the host galaxy contamination can also affect MIR luminosity-based properties (e.g., hot dust covering factors and MIR colors; [Son et al. 2022](#)). Especially for low-luminosity (e.g., $L_{5100} < 10^{44} \text{ erg s}^{-1}$) quasars, their host galaxy contributions are significant even in the optical ([Shen et al. 2011](#)).

In order to estimate the host galaxy contribution, we use the photometric data of SDSS, 2MASS PSC, and *WISE*. Note that W_4 fluxes can sporadically produce unreliable results that overemphasize IR components, and thus, are excluded in this work. We fit the photometric data, $f(\lambda)$, with a SED model. The SED model

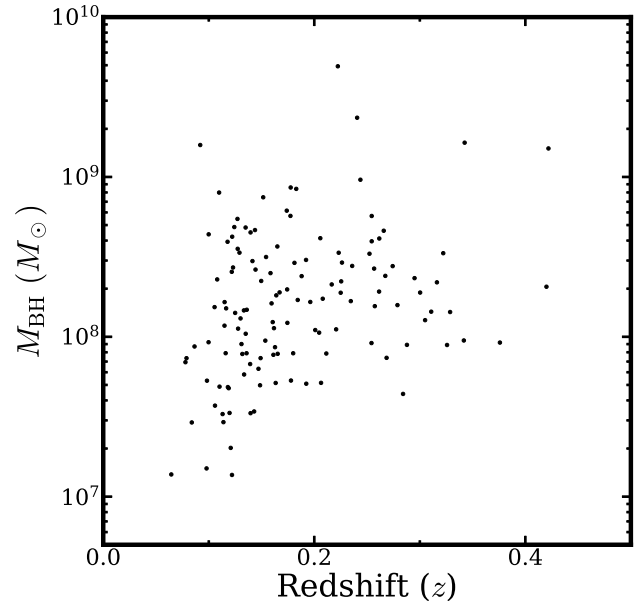


Figure 2. Redshift vs. BH mass for our sample. The BH masses are measured based on the L_{5100} and $\text{FWHM}_{\text{H}\beta}$ values ([Vestergaard & Peterson 2006](#)).

is a weighted sum of the spectra of AGN ($A(\lambda)$), elliptical galaxy ($E(\lambda)$), spiral galaxy ($S(\lambda)$), and irregular galaxy ($I(\lambda)$), which is defined as

$$f(\lambda) = C_1 A(\lambda) + C_2 E(\lambda) + C_3 S(\lambda) + C_4 I(\lambda), \quad (2)$$

where C_1 , C_2 , C_3 , and C_4 are the normalization constants of each component. The $A(\lambda)$, $E(\lambda)$, $S(\lambda)$, and $I(\lambda)$ are the reddened spectra of $A_0(\lambda)$, $E_0(\lambda)$, $S_0(\lambda)$, and $I_0(\lambda)$, respectively (see below for how the spectra were reddened). The $A_0(\lambda)$, $E_0(\lambda)$, $S_0(\lambda)$, and $I_0(\lambda)$ are the intrinsic spectral templates of AGN, elliptical galaxy, spiral galaxy, and irregular galaxy, respectively. The spectral templates of elliptical, spiral, and irregular galaxies are adopted from [Assef et al. \(2010\)](#). Note that IR emissions from star-formation are also included in these templates.

However, the AGN spectral template is adopted from [Krawczyk et al. \(2013\)](#), since the fiducial bolometric luminosity is measured based on the spectral template in [Krawczyk et al. \(2013\)](#). We note that the AGN template of [Krawczyk et al. \(2013\)](#) has a similar SED shape to those several other AGN templates (e.g., [Richards et al. 2006](#)), but differs from the AGN template of [Assef et al. \(2010\)](#), especially at wavelengths shorter than $0.1 \mu\text{m}$. However, within the $0.1\text{--}20 \mu\text{m}$ range used in our SED fitting, the difference is not significant. Hence, the measured $L_{3.4}$ and $L_{4.6}$ values are similar, and these values based on [Krawczyk et al. \(2013\)](#) are $\sim 5\%$ higher

than those from [Assef et al. \(2010\)](#), corresponding to only 0.02 dex in the logarithmic scale.

The reddened spectra are converted from the intrinsic spectra with the $E(B - V)$ values as

$$\log \left(\frac{X(\lambda)}{X_0(\lambda)} \right) = -\frac{k(\lambda)E(B - V)}{1.086}, \quad (3)$$

where $k(\lambda)$ is a reddening law from [Fitzpatrick \(1999\)](#) based on Galactic extinction curve under the assumption of $R_V = 3.1$ (e.g., [Weingartner & Draine 2001](#)). Here, we note that $X(\lambda)$ and $X_0(\lambda)$ denote the four kinds of reddened spectra and their intrinsic spectra, respectively.

Here, the different dust extinction is applied to the AGN and host galaxy components, as often done in previous studies (e.g., [Assef et al. 2010](#)). We also perform the SED fitting by applying the same dust extinction to the AGN and host galaxy templates. However, the difference in the measured MIR continuum luminosity is negligible ($< 1\%$), which is due to (i) the MIR continuum luminosity being insensitive to the dust extinction; (ii) we only use the unobscured quasars ($E(B - V) < 0.1$).

This SED fitting procedure is performed with MPFIT ([Markwardt 2009](#)) based on Interactive Data Language (IDL). Figure 3 shows examples of the photometric data with the best-fit SED model of four randomly selected SDSS quasars.

In the following sections, we use the MIR continuum luminosities measured from the best-fit SED model. The $L_{3.4}$ and $L_{4.6}$ values are defined as the measured $C_1 A_0(\lambda)$ values at 3.4 and 4.6 μm in the rest-frame, respectively.

4. EMPIRICAL RELATIONS BETWEEN L5100 AND L_{MIR}

Before establishing L_{MIR} -based L_{bol} and M_{BH} estimators, we find relations between the L5100 values and the MIR continuum luminosities. Figure 4 shows the correlations between the $L_{3.4}$ values and the L5100 values. To derive the correlations between the two quantities, we assume a nonlinear relationship as

$$\log \left(\frac{L_Y}{10^{44} \text{ erg s}^{-1}} \right) = \alpha + \beta \log \left(\frac{L_X}{10^{44} \text{ erg s}^{-1}} \right). \quad (4)$$

Here, X and Y are identifiers of the L_{MIR} and L5100, respectively. We linearly fit the two quantities in the log-log plane with two free variables, the Y intercept (α) and the slope (β). These correlations are fitted by using the CURVE_FIT procedure of the SciPy package ([Virtanen et al. 2020](#)). The fitting results are summarized in Table 1, and this table also lists the root mean

square (rms) scatters of the data with respect to the best-fit results.

Since the $L_{3.4}$ and the $L_{4.6}$ are derived based on the same AGN template ([Krawczyk et al. 2013](#)), the derived $L_{3.4}$ values are simply 1.04 times bigger than the $L_{4.6}$ value. As a consequence, the fitting results for the $L_{4.6}$ have the same β and rms scatter values as for the $L_{3.4}$ case.

First, we derive the correlations between the two quantities when the slope term β is fixed to 1, as expected in the linear relationship. The best-fit relations are shown as the red-dashed lines in Figure 4, and the derived bolometric luminosity estimators provide reasonable fits with rms scatters of 0.13 dex. This result is supported by Kendall's τ test. The Kendall's τ values in these correlations are found to be ~ 0.78 .

Second, we also find the best-fit parameters of α and β when we treat the slope term β as a free parameter. Figure 4 shows the derived best-fit relations as the blue-dotted lines, and the rms scatters are 0.13 dex. In addition, the measured Kendall's τ values are also ~ 0.78 . These results imply that there is a negligible improvement when the slope term β is set as the free parameter, since the measured β is close to 1.

Additionally, instead of using the AGN template of [Krawczyk et al. \(2013\)](#), we find the best-fit parameters with the L_{MIR} values that were derived using the AGN templates from [Richards et al. \(2006\)](#) and [Assef et al. \(2010\)](#). The found best-fit correlations are shown in Figure 4, and they are not significantly different from the results based on the AGN template of [Krawczyk et al. \(2013\)](#).

5. BOLOMETRIC LUMINOSITY ESTIMATORS

In this section, we find correlations between L_{bol} and L_{MIR} for deriving the L_{MIR} -based L_{bol} estimators. First, we find the $L_{\text{bol}}-L_{\text{MIR}}$ relations when the slope term β in Equation 4 is fixed to 1. The found best-fit relations are summarized as the parameter sets A and B in Table 2, and the best-fit $L_{\text{bol}}-L_{3.4}$ relation is shown as the red-dashed line in Figure 5. The derived L_{MIR} -based L_{bol} estimators provide reasonable fits with rms scatters of 0.13 dex, and the Kendall's τ values are found to be ~ 0.80 .

Second, we also find the best-fit parameters of α and β when we treat the slope term β as a free parameter. Figure 5 shows the derived best-fit $L_{\text{bol}}-L_{3.4}$ relation as the blue-dotted lines, and the rms scatters are 0.13 dex. In addition, the measured Kendall's τ values are also ~ 0.80 . The best-fit relations are listed as the parameter

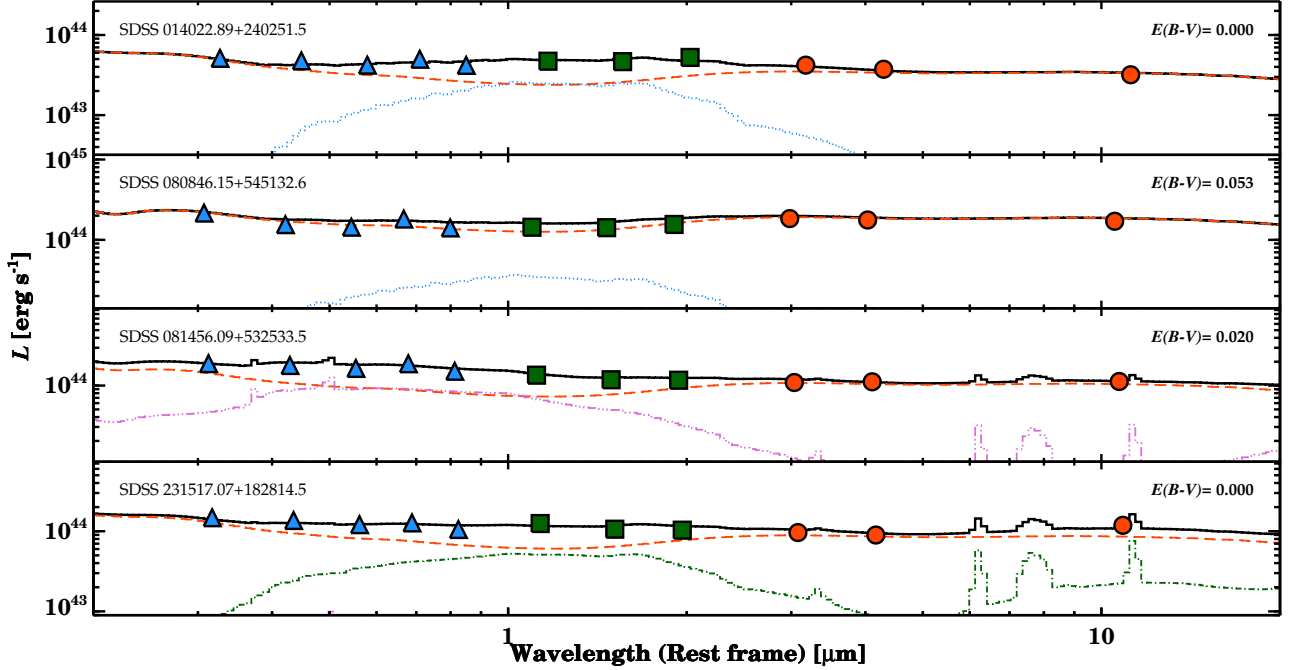


Figure 3. Photometric data of four randomly selected SDSS quasars with their best-fit SED models in the rest-frame. Blue triangles, green squares, and red circles indicate photometric data points from SDSS, 2MASS PSC, and *WISE* (*W1*, *W2*, and *W3*), respectively. The red-dashed, blue-dotted, green-dash-dotted, and purple-dash-dot-dot-dotted lines indicate the reddened AGN, elliptical galaxy, spiral galaxy, and irregular galaxy spectra, respectively. The black solid lines show the sums of the best-fit spectra. The name of the sample and the measured $E(B - V)$ value are presented on the top left and right side of each panel, respectively.

Table 1. Coefficients of the empirical relations between L_{5100} and L_{MIR} values

No.	Y	X	α	β	rms
					(dex)
A	L_{5100}	$L_{3.4}$	-0.034 ± 0.012	1 (fixed)	0.131
B	L_{5100}	$L_{4.6}$	-0.017 ± 0.012	1 (fixed)	0.131
C	L_{5100}	$L_{3.4}$	-0.008 ± 0.022	0.956 ± 0.032	0.130
D	L_{5100}	$L_{4.6}$	0.008 ± 0.022	0.956 ± 0.032	0.130

sets C and D in Table 2, and this result implies that the slope term is close to 1, even when the slope term is set as the free parameter.

Furthermore, in a manner consistent with the approach in Section 4, we derive the best-fit $L_{\text{bol}}-L_{3.4}$ relations by using the $L_{3.4}$ values obtained with the AGN templates of Richards et al. (2006) and Assef et al. (2010). The found best-fit $L_{\text{bol}}-L_{3.4}$ relations are not significantly different from those based on the AGN template of Krawczyk et al. (2013), and they are shown in Figure 5.

Additionally, we also find correlations between the bolometric luminosities and the L_{5100} values. We find

best-fit relations when the slope term β in Equation 4 is fixed to 1 or treated as a free parameter, and the derived relations are also presented as the parameter sets E and F in Table 2. Note that these results are obtained when the $1 \mu\text{m}-10 \text{keV}$ luminosity is adopted as the bolometric luminosity; hence the discrepancy arises when compared to the bolometric luminosity correction factors (e.g., 9.26; Shen et al. 2011) using different wavelength ranges (e.g., $100 \mu\text{m}-10 \text{keV}$; Richards et al. 2006).

Note that the correlations of $L_{\text{bol}}-L_{\text{MIR}}$ can be affected by the hot dust covering factor. The covering factor is known to vary from object to object (Roseboom et al. 2013; Kim et al. 2015b), and the dis-

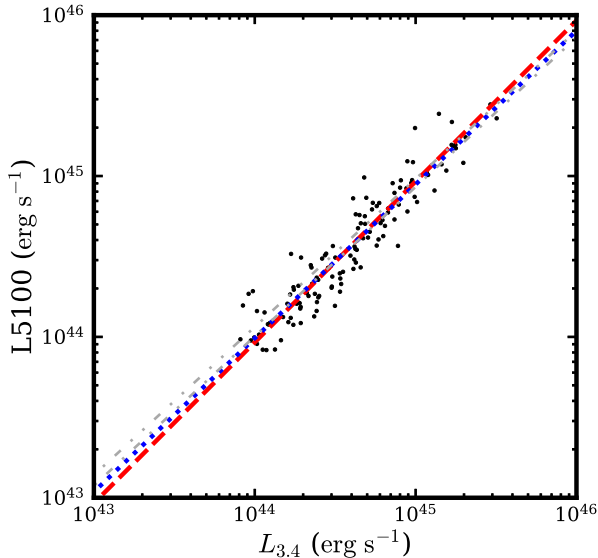


Figure 4. L5100 values versus $L_{3.4}$ values. The blue-dotted line represents the best-fit correlation when α and β in Equation 4 are set as free parameters. The red-dashed line denotes the best-fit correlation when the slope term β is fixed to 1. Gray dashed-dotted and dashed-dot-dotted lines show the best-fit correlations derived from the AGN templates of Richards et al. (2006) and Assef et al. (2010), respectively, where α and β are treated as free parameters.

tribution of the covering factor is expected to manifest as the scatters of the found relations in Table 2. Moreover, there is still a debate on the relation between the covering factor and the luminosity (e.g., Mor & Trakhtenbrot 2011; Roseboom et al. 2013; Kim et al. 2015b). For the case that the covering factor decreases with the luminosity increasing (e.g., Mor & Trakhtenbrot 2011; Roseboom et al. 2013), we expect the slope term β to be larger than the case where the dust covering factor is uniform, but the presence of the covering factor effects are not evident in the $L_{\text{bol}}-L_{\text{MIR}}$ relationships found.

Furthermore, we show that the relations of $L_{3.4}-L_{\text{bol}}$ and $L_{3.4}-L5100$ have no dependence on the redshift. To find the redshift dependence, we assumed a relationship as

$$\log(L/L_{3.4}) = \alpha + \beta \times z, \quad (5)$$

where z is redshift, and L is L_{bol} or L5100. We fit the data by setting α and β as free parameters. In the relationship with redshift, both the $L_{\text{bol}}/L_{3.4}$ and $L5100/L_{3.4}$ ratios have slope terms close to 0. Moreover, these results are consistent even when using the AGN templates of Richards et al. (2006) and Assef et al. (2010) instead of the AGN template of

Krawczyk et al. (2013). These results are shown in Figure 6.

6. BH MASS ESTIMATORS

We derive BH mass estimators based on the MIR continuum luminosities with Balmer and Paschen line FWHM values over the BH mass range of $10^{7.14}-10^{9.69} M_{\odot}$. Under the assumption that the BLRs are virialized, the BH mass can be measured as

$$M_{\text{BH}} = f \frac{R_{\text{BLR}} \Delta V^2}{G}, \quad (6)$$

where f is a scale factor depending on the geometry of the BLR, R_{BLR} is the radius of the BLR, and ΔV is the BLR velocity dispersion. Throughout this study, we use the scale factor of 5.5 (e.g., Onken et al. 2004). The R_{BLR} can be estimated directly by reverberation mapping experiment (e.g., Blandford & McKee 1982), but this experiment is difficult and expensive in time to measure. Therefore, the BH masses have been alternatively estimated from a single-epoch spectrum using empirical relations between R_{BLR} and continuum luminosity (e.g., Kaspi et al. 2000).

We derive L_{MIR} -based M_{BH} estimators that are analogous to the previous BH mass estimators based on the single-epoch method (e.g., Greene & Ho 2005; Vestergaard & Peterson 2006; Kim et al. 2010, 2015b). For the L_{MIR} -based M_{BH} estimators, the MIR continuum luminosities serve as the R_{BLR} , and the Balmer broad-line FWHM values are used as the velocity dispersion term in Equation 6. Mathematically, we need to find three unknown parameters, α , β , and γ , in the following equation:

$$\log\left(\frac{M_{\text{BH}}}{M_{\odot}}\right) = \alpha + \beta \log\left(\frac{L_{\text{X}}}{10^{44} \text{ erg s}^{-1}}\right) + \gamma \log\left(\frac{\text{FWHM}_{\text{Y}}}{10^3 \text{ km s}^{-1}}\right). \quad (7)$$

Here, X and Y are the luminosity and line identifiers, respectively. Under the virial theorem, γ is fixed to 2, and β is theoretically and empirically expected to be 0.5 (e.g., Dibai 1977; Kaspi et al. 2000; Kim et al. 2010). We adopt the fiducial BH masses from Rakshit et al. (2020) who measured the BH masses based on optical properties using the M_{BH} estimator from Vestergaard & Peterson (2006). Vestergaard & Peterson (2006) established the BH mass estimator based on the L5100 and $\text{FWHM}_{\text{H}\beta}$ with α , β , and γ of 6.91, 0.5, and 2, respectively.

Table 2. Parameters of bolometric luminosity estimators

No.	Y	X	α	β	rms
					(dex)
A	L_{bol}	$L_{3.4}$	0.718 ± 0.011	1 (fixed)	0.126
B	L_{bol}	$L_{4.6}$	0.735 ± 0.011	1 (fixed)	0.126
C	L_{bol}	$L_{3.4}$	0.722 ± 0.021	0.993 ± 0.031	0.126
D	L_{bol}	$L_{4.6}$	0.739 ± 0.021	0.993 ± 0.031	0.126
E	L_{bol}	L5100	0.752 ± 0.011	1 (fixed)	0.123
F	L_{bol}	L5100	0.764 ± 0.019	0.978 ± 0.029	0.123

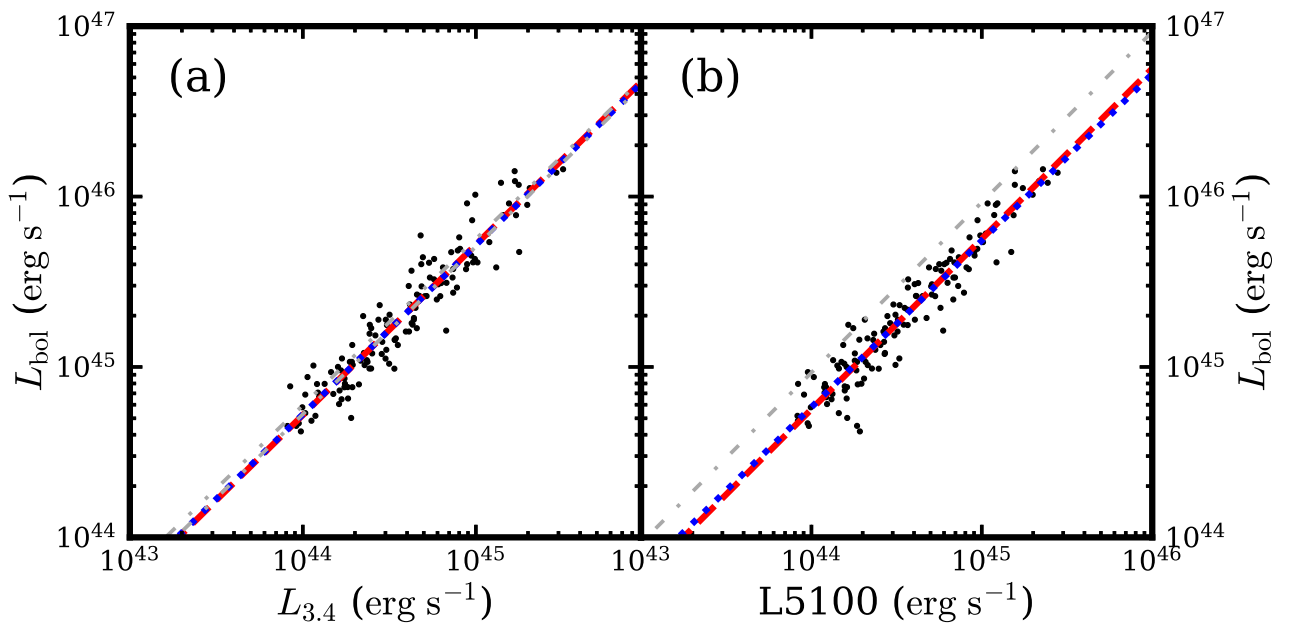


Figure 5. (a) Bolometric luminosities versus $L_{3.4}$ values. The bolometric luminosities are adopted from [Krawczyk et al. \(2013\)](#). The blue-dotted line represents the relation when α and β in Equation 4 are set as free parameters, and the red-dashed line denotes the relation when the slope term β is fixed to 1. Gray dashed-dotted and dashed-dot-dotted lines denote the best-fit correlations derived with the AGN templates of [Richards et al. \(2006\)](#) and [Assef et al. \(2010\)](#), respectively, where α and β are treated as free parameters. (b) Bolometric luminosities vs. L5100 values. The meanings of red-dashed and blue-dotted lines are identical to those in the left panel. Gray dashed-dotted line shows the relation of L5100– L_{bol} by adopting the correction factor of 9.26 ([Shen et al. 2011](#)), which is measured based on the AGN template of [Richards et al. \(2006\)](#). The discrepancy between the red-dashed and blue-dotted lines is due to [Richards et al. \(2006\)](#) using a different wavelength range ($100 \mu\text{m}$ – 10keV) for measuring the bolometric luminosity from that used ($1 \mu\text{m}$ – 10keV) by [Krawczyk et al. \(2013\)](#).

6.1. L_{MIR} -based M_{BH} estimators with Balmer line FWHM values

First, we derive L_{MIR} -based M_{BH} estimators with the $\text{FWHM}_{\text{H}\beta}$ by simply replacing the L5100 of the BH mass estimator of [Vestergaard & Peterson \(2006\)](#) with the MIR continuum luminosities. In order to replace the L5100 of the BH mass estimator, we use the L5100– L_{MIR} relations in Table 1.

We obtain the L_{MIR} -based BH mass estimators when we use the parameter sets A and B in Table 1 as the L5100– L_{MIR} relation. We find that these L_{MIR} -based BH mass estimators reproduce the M_{BH} with rms scatterers of ~ 0.07 dex. The derived L_{MIR} -based BH mass estimators are presented as the parameter sets A and B in Table 3, and Figure 7 shows the comparisons of the M_{BH} values based on the L5100 ([Vestergaard & Peterson 2006](#)) and the $L_{3.4}$ -based BH masses. Note that we omit

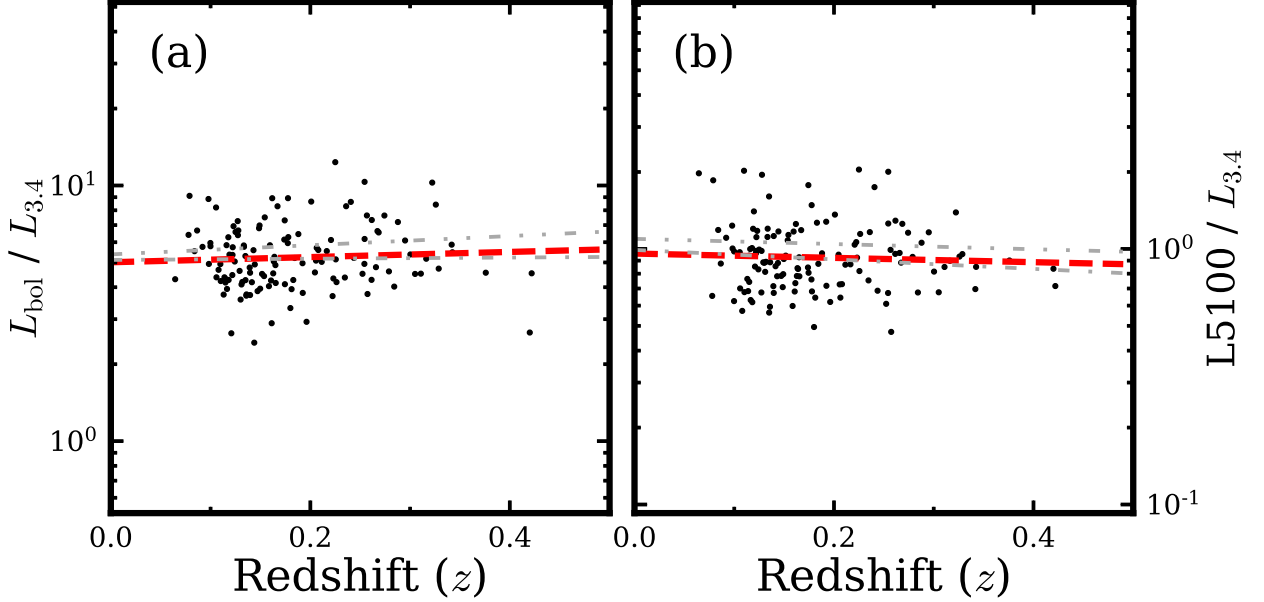


Figure 6. (a) Comparison between $L_{\text{bol}}/L_{3.4}$ and redshift. The red-dashed line denotes the best-fit relationship when α and β in Equation 5 are set as free parameters. The gray dashed-dotted and dashed-dot-dotted lines represent the best-fit correlations derived with the AGN templates of Richards et al. (2006) and Assef et al. (2010), respectively, where all parameters are treated as free parameters. (b) $L5100/L_{3.4}$ vs. redshift. The meanings of the lines are identical to those in the left panel.

Table 3. Parameters of BH mass estimators

No.	X	Y	α	β	γ	L5100- L_{MIR} relation	rms
						No. in Table 1	(dex)
A	$L_{3.4}$	H β	6.893 ± 0.021	0.5	2	A	0.066
B	$L_{4.6}$	H β	6.902 ± 0.021	0.5	2	B	0.066
C	$L_{3.4}$	H β	6.906 ± 0.023	0.478 ± 0.016	2	C	0.065
D	$L_{4.6}$	H β	6.914 ± 0.023	0.478 ± 0.016	2	D	0.065
E	$L_{3.4}$	H α	6.952 ± 0.059	0.5	2.06 ± 0.06	A	0.204
F	$L_{4.6}$	H α	6.960 ± 0.059	0.5	2.06 ± 0.06	B	0.204
G	$L_{3.4}$	H α	6.964 ± 0.060	0.478 ± 0.016	2.06 ± 0.06	C	0.204
H	$L_{4.6}$	H α	6.973 ± 0.060	0.478 ± 0.016	2.06 ± 0.06	D	0.204
I	$L_{3.4}$	P β	7.119 ± 0.069	0.5	1.790 ± 0.136	A	0.266
J	$L_{4.6}$	P β	7.128 ± 0.069	0.5	1.790 ± 0.136	B	0.266
K	$L_{3.4}$	P α	7.103 ± 0.077	0.5	2.034 ± 0.160	A	0.478
L	$L_{4.6}$	P α	7.112 ± 0.077	0.5	2.034 ± 0.160	B	0.478

to show the comparison with the $L_{4.6}$ -based BH masses, since the $L_{3.4}$ - and $L_{4.6}$ -based BH mass estimators have the exact same β , γ , and scatter.

Moreover, we obtain the L_{MIR} -based BH mass estimators when the parameter sets C and D in Table 1 is adopted as the L5100- L_{MIR} relation. The rms scatters from the L_{MIR} -based BH masses are ~ 0.07 dex, and the L_{MIR} -based BH mass estimators are presented as the parameter sets C and D in Table 3. Figure 7 also

shows the comparisons of the M_{BH} values from the optical properties (Vestergaard & Peterson 2006) and the above L_{MIR} -based BH masses.

Second, we also obtain the L_{MIR} -based M_{BH} estimators with the $\text{FWHM}_{\text{H}\alpha}$ by replacing the $\text{FWHM}_{\text{H}\beta}$ of the found L_{MIR} -based M_{BH} estimators with the $\text{FWHM}_{\text{H}\alpha}$, and the parameter sets A, B, C, and D in Table 3 are used as the $\text{FWHM}_{\text{H}\beta}$ -based M_{BH} estimators. For replacing the $\text{FWHM}_{\text{H}\beta}$, we adopt the $\text{FWHM}_{\text{H}\beta}$ -

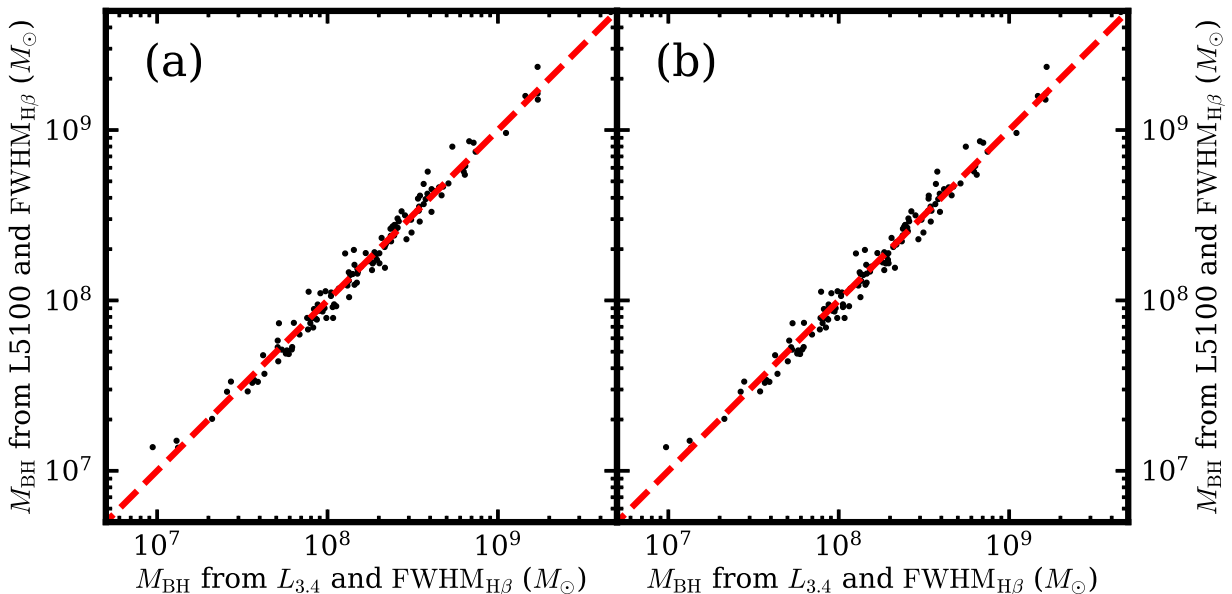


Figure 7. (a) BH masses measured from L5100 and $\text{FWHM}_{\text{H}\beta}$ versus M_{BH} values from $L_{3.4}$ and $\text{FWHM}_{\text{H}\beta}$. The L_{MIR} -based M_{BH} estimator is derived by replacing the L5100 of the M_{BH} estimator of Vestergaard & Peterson (2006) with the $L_{3.4}$. For replacing the L5100 of the M_{BH} estimator, we use the linear relation of L5100– L_{MIR} presented as the parameter set A in Table 1. The red-dashed line represents the case where the BH masses are identical. (b) Comparison of M_{BH} values derived from the optical properties and the $L_{3.4}$ -based BH masses. The $L_{3.4}$ -based BH masses are measured as the left panel, but the parameter set C in Table 1 is used for the L5100– L_{MIR} relation. The meaning of the red-dashed line is identical to that in the left panel.

$\text{FWHM}_{\text{H}\alpha}$ relation in Greene & Ho (2005), which is

$$\frac{\text{FWHM}_{\text{H}\beta}}{1000 \text{ km s}^{-1}} = (1.07 \pm 0.07) \times \left(\frac{\text{FWHM}_{\text{H}\alpha}}{1000 \text{ km s}^{-1}} \right)^{(1.03 \pm 0.03)} \quad (8)$$

The derived L_{MIR} -based M_{BH} estimators with the $\text{FWHM}_{\text{H}\alpha}$ are presented as the parameter sets E, F, G, and H in Table 3, and they can reproduce the BH masses with rms scatters of ~ 0.20 dex that is dominated by the rms scatter in the $\text{FWHM}_{\text{H}\beta}$ – $\text{FWHM}_{\text{H}\alpha}$ relation (Greene & Ho 2005).

6.2. L_{MIR} -based M_{BH} estimators with Paschen line FWHM values

Here, we obtain BH mass estimators by replacing the $\text{FWHM}_{\text{H}\beta}$ of the L_{MIR} -based M_{BH} estimators with the Paschen line FWHM values. Some extremely dust-obscured quasars have only narrow line components in their Balmer lines, but their Paschen lines can have broad-line components. Hence, we expect that the BH mass estimators with the Paschen line FWHM values can be applied for studying heavily obscured quasars when their IR spectroscopic data are obtained.

For deriving the BH mass estimators, we need the Paschen line FWHM values. The Paschen line FWHM values can be obtained by using empirical relations

between the Balmer and Paschen line FWHM values. Kim et al. (2010) found the empirical relations with 37 unobscured type 1 AGNs at low- z ($z < 0.4$) by performing a linear bisector fit, and the found relations were presented in the form of

$$\log \left(\frac{\text{FWHM}_{\text{H}\beta}}{1000 \text{ km s}^{-1}} \right) = \alpha + \beta \log \left(\frac{\text{FWHM}_{\text{Paschen}}}{1000 \text{ km s}^{-1}} \right). \quad (9)$$

The derived α and β values for the $\text{P}\beta$ line are 0.113 ± 0.033 and 0.895 ± 0.068 , and the $\text{P}\alpha$ line are 0.105 ± 0.037 and 1.017 ± 0.080 , respectively.

Using the relations between the $\text{FWHM}_{\text{H}\beta}$ and $\text{FWHM}_{\text{Paschen}}$, we convert the parameter sets A and B in Table 3 by replacing the $\text{FWHM}_{\text{H}\beta}$ with the $\text{FWHM}_{\text{P}\beta}$ and the $\text{FWHM}_{\text{P}\alpha}$. Finally, we obtain four BH mass estimators with the Paschen line FWHM values. The obtained BH mass estimators are expressed as Equation 7, and the derived α , β , and γ coefficients are listed as the parameter sets I, J, K, and L in Table 3.

7. DISCUSSION

7.1. Host galaxy contamination

In this subsection, we examine the host galaxy contamination in the L_{IR} values. We measure the host contamination by fitting SED model as performed in Section 3, and the host contamination at a given wavelength

is defined as

$$\text{Host galaxy contamination } (\lambda) = \frac{C_2 E_0(\lambda) + C_3 S_0(\lambda) + C_4 I_0(\lambda)}{C_1 A_0(\lambda) + C_2 E_0(\lambda) + C_3 S_0(\lambda) + C_4 I_0(\lambda)}. \quad (10)$$

We measure the host contamination at 1.2, 1.7, 2.2, 3.4, 4.6, and 12 μm in the rest-frame. Figure 8 shows the median host contamination of our sample. The host contamination is significant ($> 20\%$; up to $\sim 50\%$) at 1.2, 1.7, and 2.2 μm , but it becomes negligible ($< 20\%$) at 3.4, 4.6, and 12 μm .

The host contamination is found to be very low ($< 10\%$) at 12 μm . Our host galaxy SED templates contain the reprocessed IR emission from star-formation, but the host contamination at $> 12 \mu\text{m}$ may be underestimated if there is a more significant star-formation activity in the host galaxy than the template galaxy SEDs. On the other hand, the MIR emission contribution from star-formation is relatively weak at 3.4 and 4.6 μm , so we expect that the star-formation does not affect the measured host contamination at 3.4 and 4.6 μm .

In addition, the host contamination at 1.2, 1.7, and 2.2 μm are found to be higher than 20%. This result remains unchanged even when using the AGN template of Richards et al. (2006), which is due to that the stellar radiation peaks at these wavelengths. Note that these measurements can increase ($\gtrsim 40\%$; up to $\sim 70\%$) when the AGN template is adopted from Assef et al. (2010). The AGN SED template in Assef et al. (2010) is weaker at 1 μm than other AGN templates (e.g., Elvis et al. 1994; Richards et al. 2006; Krawczyk et al. 2013), and it is suspected to yield the overestimated host contamination at optical and NIR. Hickox et al. (2017) also reported this issue. They measured the host contamination at 1 μm , and found it $\sim 75\%$ when using the AGN template of Assef et al. (2010). However, the host contamination decreases to $\sim 50\text{--}60\%$ with the AGN template of Richards et al. (2006). Moreover, Richards et al. (2006) measured the host contamination at 1.6 μm , and it is found to be only $\sim 30\text{--}40\%$. Therefore, the host contamination measurements at optical and NIR can be somewhat increased when using the AGN template of Assef et al. (2010).

7.2. Do SDSS quasars suffer from dust extinction?

In this subsection, we compare the L_{bol} and M_{BH} values measured using the MIR continuum luminosity-based estimators to those derived based on the L5100 values to investigate how much SDSS quasars may suffer from the dust extinction. For this comparison, we use the sample selected from the similar criteria described in Section 2, excepting for the Balmer decrement and

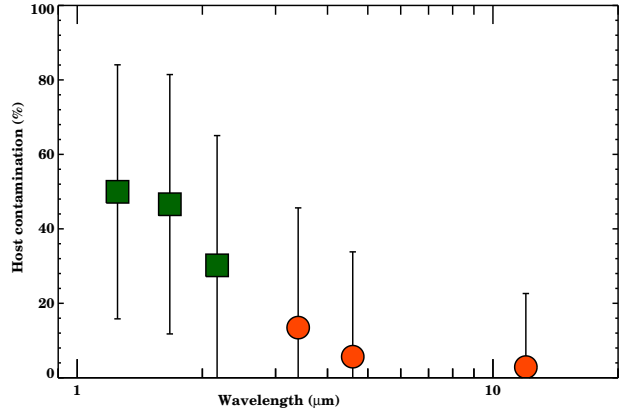


Figure 8. Host galaxy contamination at 1.2, 1.7, 2.2, 3.4, 4.6, and 12 μm in the rest-frame. Green squares denote the measured host contamination at 1.2, 1.7, and 2.2 μm , and red circles mean those at 3.4, 4.6, and 12 μm .

$E(B - V)$ limits. We finally take 242 low- z ($z \lesssim 0.5$) SDSS quasars, and they have wide ranges of BH mass ($10^{7.07} M_{\odot} < M_{\text{BH}} < 10^{9.69} M_{\odot}$) and bolometric luminosity ($10^{44.33} \text{ erg s}^{-1} < L_{\text{bol}} < 10^{46.16} \text{ erg s}^{-1}$).

We measure the L_{bol} and M_{BH} values using the L_{MIR} -based estimators ($L_{\text{bol,MIR}}$ and $M_{\text{BH,MIR}}$ values, hereafter). The $L_{\text{bol,MIR}}$ and $M_{\text{BH,MIR}}$ values are derived by using the parameter set B in Table 2 and B in Table 3, respectively. Furthermore, we adopt the L_{bol} and M_{BH} values based on L5100 values. We denote them as $L_{\text{bol,opt}}$ and $M_{\text{BH,opt}}$ hereafter. The $L_{\text{bol,opt}}$ values were measured by using the parameter set E in Table 2, and the $M_{\text{BH,opt}}$ values were measured with the L5100 and $\text{FWHM}_{\text{H}\beta}$ values (Vestergaard & Peterson 2006) as described in Section 2.

Figure 9 shows comparisons of these properties, implying that some SDSS quasars suffer from dust extinction. A non-negligible fraction (16%) of the sample possesses $L_{\text{bol,MIR}} > 1.5 \times L_{\text{bol,opt}}$. Considering the $L_{\text{bol,MIR}}$ measurement is relatively immune from the dust extinction effects, these $L_{\text{bol,opt}}$ values are expected to be underestimated. For M_{BH} , the underestimation from optical measurements is less serious than L_{bol} since M_{BH} is proportional to $L^{0.5}$ rather than L of L_{bol} . Nevertheless, $M_{\text{BH,opt}}$ values of 16% of the SDSS quasars are underestimated by a factor of 1.22 ($\sim \sqrt{1.5}$) or more. The Eddington ratio is also proportional to $L^{0.5}$ for both optical and MIR luminosity-based estimators, so the optically derived Eddington ratios (λ_{Edd}) are less than 80% of the MIR-derived λ_{Edd} for 14% of the SDSS quasars.

Furthermore, we compare the $L_{\text{bol,MIR}}$ values to the $L_{\text{bol,opt}}$ values, as functions of two dust extinction indicators, $\log(L_{\text{H}\alpha}/L_{\text{H}\beta})$ and AGN optical power-law slope, and the results are shown in Figure 10. To clarify trends of $L_{\text{bol,MIR}}/L_{\text{bol,opt}}$, we divide them into three

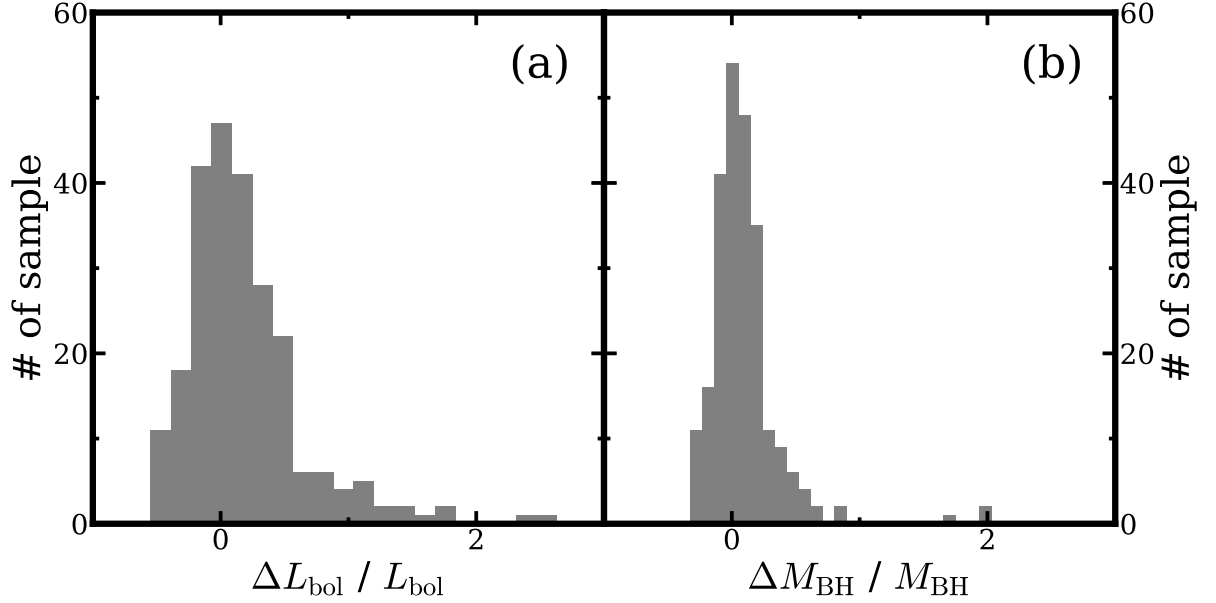


Figure 9. (a) Comparison of L_{bol} derived from the $L_{4.6}$ vs. L_{bol} measured based on the L5100. The gray histogram represents the distribution of $\Delta L_{\text{bol}}/L_{\text{bol}}$, which is $(L_{\text{bol,MIR}} - L_{\text{bol,opt}})/L_{\text{bol,opt}}$, and its distribution is clearly skewed toward higher values. (b) Comparison of M_{BH} measured from the $L_{4.6}$ and the L5100. The gray histogram shows the distribution of $\Delta M_{\text{BH}}/M_{\text{BH}}$, which is $(M_{\text{BH,MIR}} - M_{\text{BH,opt}})/M_{\text{BH,opt}}$, which are somewhat skewed toward higher values.

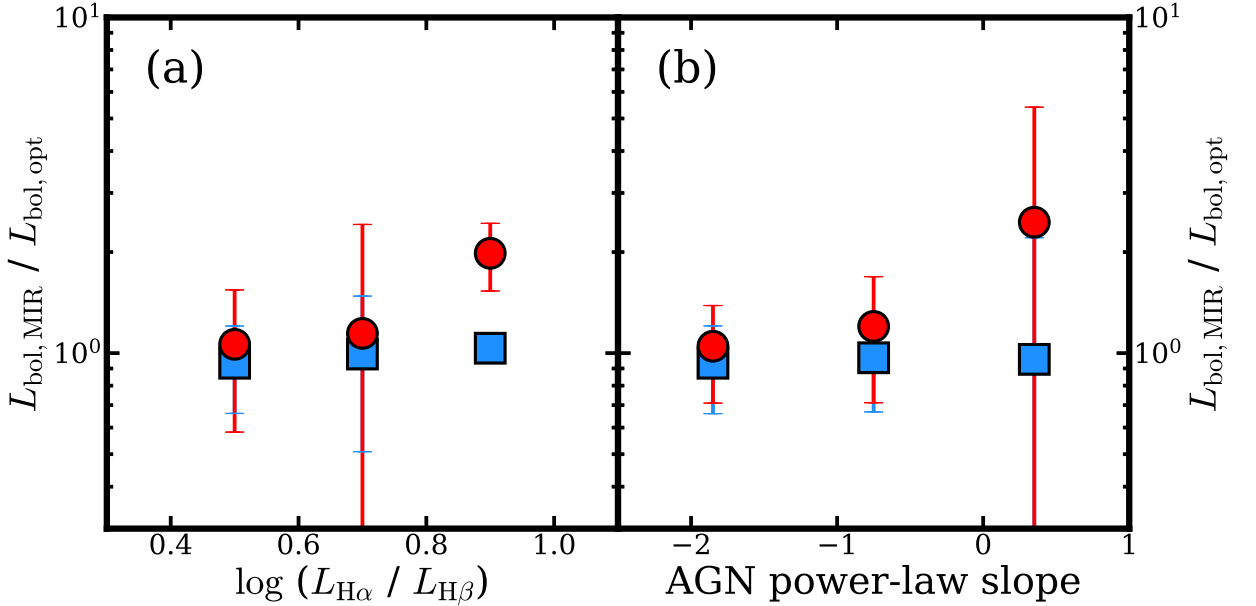


Figure 10. (a) $L_{\text{bol,MIR}}/L_{\text{bol,opt}}$ along with $\log(L_{\text{H}\alpha}/L_{\text{H}\beta})$. Red circles represent the $L_{\text{bol,MIR}}/L_{\text{bol,opt}}$, and blue squares the dust extinction-corrected $L_{\text{bol,MIR}}/L_{\text{bol,opt}}$. (b) $L_{\text{bol,MIR}}/L_{\text{bol,opt}}$ along with AGN power-law slope. The meanings of red circles and blue squares are identical.

bins of $\log(L_{\text{H}\alpha}/L_{\text{H}\beta})$: 0.4~0.6, 0.6~0.8, and 0.8~1.0; and the AGN power-law slope: -2.4~-1.3, -1.3~-0.2, and -0.2~-0.9.

For the comparisons, the $L_{\text{H}\beta}$, $L_{\text{H}\alpha}$, and AGN optical power-law slope values are adopted from Rakshit et al. (2020). Here, the $L_{\text{H}\beta}$ and $L_{\text{H}\alpha}$ represent the H β and H α broad-line luminosities, respectively. The AGN power-law slope is measured by fitting a simple power-law function of $f_\lambda \propto \lambda^\alpha$ to the optical spectra, and the fitted α is defined as the AGN power-law slope.

If the dust extinction plays a significant role in the large deviation in $L_{\text{bol,MIR}}$ and $M_{\text{BH,MIR}}$ from the optically derived values, we expect that the deviation becomes stronger as the dust extinction becomes stronger as indicated by these two dust extinction indicators. Figure 10 shows the $L_{\text{bol,MIR}}/L_{\text{bol,opt}}$ as a function of $\log(L_{\text{H}\alpha}/L_{\text{H}\beta})$ and AGN power-law slope. Note that the average $\log(L_{\text{H}\alpha}/L_{\text{H}\beta})$ and AGN power-law slope of unobscured quasars were found to be ≈ 0.5 (e.g., Dong et al. 2008) and ≈ -1.5 (e.g., Vanden Berk et al. 2001), respectively. We find that $L_{\text{bol,MIR}}/L_{\text{bol,opt}}$ increases by over two times when $\log(L_{\text{H}\alpha}/L_{\text{H}\beta}) \gtrsim 0.8$ and the AGN power-law slope is $\gtrsim -0.2$. Figure 10 clearly shows such a trend, supporting the idea that some of the SDSS quasars suffer from the dust extinction, and their $L_{\text{bol,opt}}$ and $M_{\text{BH,opt}}$ values can be underestimated without applying dust extinction correction.

We note that low-luminosity quasars and intermediate-type AGNs also have the high $L_{\text{H}\alpha}/L_{\text{H}\beta}$ and AGN power-law slope. However, the SDSS quasars are bright ($10^{44.33} \text{ erg s}^{-1} < L_{\text{bol}} < 10^{46.16} \text{ erg s}^{-1}$) type 1 quasars. A significant majority ($\sim 90\%$) of the SDSS quasars have the broad component (FWHM $> 2000 \text{ km s}^{-1}$) in the H β and H α lines. Therefore, the dust extinction is strongly suspected to yield the trends found in Figure 10.

We also check if dust extinction correction can bring $L_{\text{bol,MIR}}/L_{\text{bol,opt}}$ to the values close to one. In order to correct the dust extinction, we use the $E(B-V)$ values measured by the SED fitting as described in Section 3, and the dust reddening law (Fitzpatrick 1999) under the assumption of $R_V = 3.1$ (e.g., Weingartner & Draine 2001). After correcting the dust extinction for the $L_{\text{bol,opt}}$, the newly measured $L_{\text{bol,MIR}}/L_{\text{bol,opt}}$ is found to be ~ 1 , even at $\log(L_{\text{H}\alpha}/L_{\text{H}\beta}) \gtrsim 0.8$ and AGN power-law slope $\gtrsim -0.2$. This result also demonstrates the importance of dust extinction correction when deriving key AGN physical quantities, just like dust extinction needs to properly taken into account when deriving star-formation rates of dusty galaxies (e.g., Shim et al. 2013). To first approximation, a rough correction based on $E(B-V)$ values from SED fittings may be sufficient,

although we expect that our MIR estimates provide more accurate values of L_{bol} and M_{BH} when $E(B-V)$ values are uncertain.

Note that we will provide the L_{bol} and M_{BH} values derived from the MIR continuum luminosity-based estimators for SDSS quasars in a future work. We expect that the newly provided L_{bol} and M_{BH} values will be useful for investigating the nature of quasars without the effects of dust extinction.

8. SUMMARY

We derive the L_{bol} and M_{BH} estimators using the MIR continuum luminosities, $L_{3.4}$ and $L_{4.6}$. Since these MIR continuum luminosities are (i) relatively immune from dust extinction effects; and (ii) measurable from IR photometric data that are largely available in public domain, we expect the L_{MIR} -based L_{bol} and M_{BH} estimators will be extensively used for studying various types of dust-obscured quasars. In particular, it will be useful for interpreting the data from current and future space IR telescopes, James-Webb Space Telescope (*JWST*) and the Spectro-Photometer for the History of the Universe, Epoch of Reionization, and Ices Explorer (SPHEREx), where the IR continua and broad lines may be detectable for obscured AGNs.

The derived L_{MIR} -based L_{bol} and M_{BH} estimators allow the determinations of L_{bol} and M_{BH} at an accuracy of $\lesssim 0.2$ dex with respect to the values derived from optical spectra for unobscured quasars. We also derive the M_{BH} estimators with the Paschen line FWHM values for possible applications for heavily dust-obscured quasars that have no broad-line components in their Balmer lines.

We apply the derived MIR continuum luminosity-based L_{bol} and M_{BH} estimators for the SDSS quasars at low- z ($\lesssim 0.5$). We find that the derived L_{bol} values using MIR data are significantly higher (> 1.5 times) than those from optical luminosity-based estimators for $\sim 15\%$ of the SDSS quasars. Such a trend is visible for M_{BH} to some degree too. We also show that a clear correlation exists between the L_{bol} underestimates and the degree of dust extinction, suggesting the dust extinction is responsible for the L_{bol} underestimates. Our results imply that a non-negligible fraction of SDSS quasars are dust obscured, and their properties should be measured by the estimators that are relatively immune from dust extinction, such as the MIR continuum and the IR hydrogen line (Kim et al. 2010, 2015b, 2020) based estimators, or at least be corrected based on the dust extinction parameters that are measurable in optical.

There will be a wealth of MIR data available for both close, bright quasars and faint, distant quasars from the

current and upcoming space missions such as *JWST* and SPHEREx. Therefore, the L_{MIR} -based estimators can be extensively applied for studying dust-obscured quasars with the data from such space missions.

1 We thank the anonymous referee for the useful com-
2 ments. This work was supported by Pusan National
3 University Research Grant, 2020. D.K. acknowledges
4 the support of the National Research Foundation of
5 Korea (NRF) grant (Nos. 2021R1C1C1013580 and
6 2022R1A4A3031306) funded by the Korean Government
7 (MSIT). M.I. acknowledges the support from the Na-
8 tional Research Foundation of Korea (NRF) grants Nos.
9 2020R1A2C3011091 and 2021M3F7A1084525, funded
10 by the Korean Government (MSIT). M.K. acknowl-
11 edges the support by the National Research Founda-
12 tion of Korea (NRF) grant (No. 2022R1A4A3031306).
13 Y.K. was supported by the National Research Foun-
14 dation of Korea (NRF) grant funded by the Korean
15 Government (MSIT) (Nos. 2021R1C1C2091550 and
16 2022R1A4A3031306).

Software: FM_UNRED (Fitzpatrick 1999), MPFIT (Markwardt 2009), SciPy (Virtanen et al. 2020),

REFERENCES

- Anderson, S. F., Voges, W., Margon, B., et al. 2003, *AJ*, 126, 2209
- Antonucci, R. 1993, *ARA&A*, 31, 473
- Assef, R. J., Kochanek, C. S., Brodwin, M., et al. 2010, *ApJ*, 713, 970
- Barvainis, R. 1987, *ApJ*, 320, 537
- Becker, R. H., White, R. L., Gregg, M. D., et al. 2001, *ApJS*, 135, 227
- Bennert, V. N., Treu, T., Woo, J.-H., et al. 2010, *ApJ*, 708, 1507
- Bentz, M. C., Peterson, B. M., Pogge, R. W., et al. 2009, *ApJL*, 694, L166
- Blandford, R. D. & McKee, C. F. 1982, *ApJ*, 255, 419
- Bruzual, G. & Charlot, S. 2003, *MNRAS*, 344, 1000
- Comastri, A., Fiore, F., Vignali, C., et al. 2001, *MNRAS*, 327, 781
- Croom, S. M., Smith, R. J., Boyle, B. J., et al. 2004, *MNRAS*, 349, 1397
- Cutri, R. M., Nelson, B. O., Kirkpatrick, J. D., et al. 2001, *The New Era of Wide Field Astronomy*, 232, 78
- Cutri, R. M., Skrutskie, M. F., van Dyk, S., et al. 2003, “The IRSA 2MASS All-Sky Point Source Catalog, NASA/IPAC Infrared Science Archive”
- Cutri, R. M., Wright, E. L., Conrow, T., et al. 2021, *VizieR Online Data Catalog*, II/328
- Dibai, E. A. 1977, *Soviet Astronomy Letters*, 3, 1
- Dong, X., Wang, T., Wang, J., et al. 2008, *MNRAS*, 383, 581
- Eisenhardt, P. R. M., Wu, J., Tsai, C.-W., et al. 2012, *ApJ*, 755, 173
- Elitzur, M. 2012, *ApJL*, 747, L33
- Elvis, M., Wilkes, B. J., McDowell, J. C., et al. 1994, *ApJS*, 95, 1
- Ferrarese, L., & Merritt, D. 2000, *ApJL*, 539, L9
- Fitzpatrick, E. L. 1999, *PASP*, 111, 63
- Gallagher, S. C., Richards, G. T., Lacy, M., et al. 2007, *ApJ*, 661, 30
- Gebhardt, K., Bender, R., Bower, G., et al. 2000, *ApJL*, 539, L13
- Georgakakis, A., Clements, D. L., Bendo, G., et al. 2009, *MNRAS*, 394, 533
- Glikman, E., Helfand, D. J., & White, R. L. 2006, *ApJ*, 640, 579
- Glikman, E., Helfand, D. J., White, R. L., et al. 2007, *ApJ*, 667, 673
- Glikman, E., Simmons, B., Maily, M., et al. 2015, *ApJ*, 806, 218
- Graham, A. W. 2007, *MNRAS*, 379, 711
- Graham, A. W., & Driver, S. P. 2007, *ApJ*, 655, 77
- Graham, A. W., Erwin, P., Caon, N., et al. 2001, *ApJL*, 563, L11
- Grazian, A., Cristiani, S., D’Odorico, V., Omizzolo, A., & Pizzella, A. 2000, *AJ*, 119, 2540
- Greene, J. E., & Ho, L. C. 2005, *ApJ*, 630, 122
- Greene, J. E., Peng, C. Y., Kim, M., et al. 2010, *ApJ*, 721, 26
- Guo, H., Liu, X., Shen, Y., et al. 2019, *MNRAS*, 482, 3288
- Gültekin, K., Richstone, D. O., Gebhardt, K., et al. 2009, *ApJ*, 698, 198
- Haas, M., Klaas, U., Müller, S. A. H., et al. 2003, *A&A*, 402, 87
- Hamann, F., Zakamska, N. L., Ross, N., et al. 2017, *MNRAS*, 464, 3431
- Hickox, R. C., Myers, A. D., Greene, J. E., et al. 2017, *ApJ*, 849, 53
- Hopkins, P. F., Hernquist, L., Cox, T. J., et al. 2005, *ApJ*, 630, 705
- Hopkins, P. F., Hernquist, L., Cox, T. J., et al. 2006, *ApJS*, 163, 1
- Hopkins, P. F., Hernquist, L., Cox, T. J., & Kereš, D. 2008, *ApJS*, 175, 356
- Ichikawa, K., Ricci, C., Ueda, Y., et al. 2019, *ApJ*, 870, 31
- Im, M., Griffiths, R. E., & Ratnatunga, K. U. 1997, *ApJ*, 475, 457
- Im, M., Lee, I., Cho, Y., et al. 2007, *ApJ*, 664, 64
- Kaspi, S., Smith, P. S., Netzer, H., et al. 2000, *ApJ*, 533, 631
- Kaspi, S., Maoz, D., Netzer, H., et al. 2005, *ApJ*, 629, 61
- Kim, D., Im, M., & Kim, M. 2010, *ApJ*, 724, 386
- Kim, D., Im, M., Glikman, E., et al. 2015a, *ApJ*, 812, 66
- Kim, D., Im, M., Kim, J. H., et al. 2015b, *ApJS*, 216, 17
- Kim, D. & Im, M. 2018, *A&A*, 610, A31
- Kim, D., Im, M., Canalizo, G., et al. 2018, *ApJS*, 238, 37
- Kim, D., Im, M., Kim, M., et al. 2020, *ApJ*, 894, 126
- Kim, D., Lee, D., & Im, M. 2022, *MNRAS*, 509, 1147
- Kormendy, J., & Ho, L. C. 2013, *ARA&A*, 51, 511
- Krawczyk, C. M., Richards, G. T., Mehta, S. S., et al. 2013, *ApJS*, 206, 4
- Lanz, L., Hickox, R. C., Baloković, M., et al. 2019, *ApJ*, 870, 26
- Lee, I., Im, M., Kim, M., et al. 2008, *ApJS*, 175, 116
- Lyke, B. W., Higley, A. N., McLane, J. N., et al. 2020, *ApJS*, 250, 8
- Lynden-Bell, D. 1969, *Nature*, 223, 690
- Maddox, N. & Hewett, P. C. 2006, *MNRAS*, 367, 717
- Mainzer, A., Bauer, J., Grav, T., et al. 2011, *ApJ*, 731, 53
- Markwardt, C. B. 2009, *Astronomical Data Analysis Software and Systems XVIII*, 411, 251

- Menci, N., Cavaliere, A., Fontana, A., et al. 2004, *ApJ*, 604, 12
- Mor, R. & Trakhtenbrot, B. 2011, *ApJL*, 737, L36
- Netzer, H., Lutz, D., Schweitzer, M., et al. 2007, *ApJ*, 666, 806
- Onken, C. A., Ferrarese, L., Merritt, D., et al. 2004, *ApJ*, 615, 645
- Pâris, I., Petitjean, P., Aubourg, É., et al. 2014, *A&A*, 563, A54
- Pâris, I., Petitjean, P., Aubourg, É., et al. 2018, *A&A*, 613, A51
- Peterson, B. M., Ferrarese, L., Gilbert, K. M., et al. 2004, *ApJ*, 613, 682
- Planck Collaboration, Ade, P. A. R., Aghanim, N., et al. 2016, *A&A*, 594, A13
- Polletta, M., Weedman, D., Hönig, S., et al. 2008, *ApJ*, 675, 960-984
- Puchnarewicz, E. M., & Mason, K. O. 1998, *MNRAS*, 293, 243
- Rakshit, S., Stalin, C. S., & Kotilainen, J. 2020, *ApJS*, 249, 17
- Richards, G. T., Hall, P. B., Vanden Berk, D. E., et al. 2003, *AJ*, 126, 1131
- Richards, G. T., Lacy, M., Storrie-Lombardi, L. J., et al. 2006, *ApJS*, 166, 470
- Risaliti, G., & Elvis, M. 2005, *ApJL*, 629, L17
- Rose, M. 2014, American Astronomical Society Meeting Abstracts #223, 223, #321.03
- Rose, M., Tadhunter, C. N., Holt, J., & Rodríguez Zaurín, J. 2013, *MNRAS*, 432, 2150
- Roseboom, I. G., Lawrence, A., Elvis, M., et al. 2013, *MNRAS*, 429, 1494
- Ruiz, A., Della Ceca, R., Caccianiga, A., Severgnini, P., & Carrera, F. 2014, *The X-ray Universe 2014*, 314
- Runnoe, J. C., Brotherton, M. S., & Shang, Z. 2012, *MNRAS*, 422, 478
- Sanders, D. B., Soifer, B. T., Elias, J. H., et al. 1988, *ApJ*, 325, 74
- Sanders, D. B., & Mirabel, I. F. 1996, *ARA&A*, 34, 749
- Schneider, D. P., Hall, P. B., Richards, G. T., et al. 2005, *AJ*, 130, 367
- Shen, Y., Richards, G. T., Strauss, M. A., et al. 2011, *ApJS*, 194, 45
- Shen, Y., Hall, P. B., Horne, K., et al. 2019, *ApJS*, 241, 34
- Shim, H., Im, M., Ko, J., et al. 2013, *ApJS*, 207, 37
- Son, S., Kim, M., & Ho, L. C. 2022, *ApJ*, 927, 107
- Stanley, F., Alexander, D. M., Harrison, C. M., et al. 2017, *MNRAS*, 472, 2221
- Steffen, A. T., Strateva, I., Brandt, W. N., et al. 2006, *AJ*, 131, 2826
- Suganuma, M., Yoshii, Y., Kobayashi, Y., et al. 2006, *ApJ*, 639, 46
- Tozzi, P., Gilli, R., Mainieri, V., et al. 2006, *A&A*, 451, 457
- Tremaine, S., Gebhardt, K., Bender, R., et al. 2002, *ApJ*, 574, 740
- Urrutia, T., Lacy, M., & Becker, R. H. 2008, *ApJ*, 674, 80-96
- Urrutia, T., Becker, R. H., White, R. L., et al. 2009, *ApJ*, 698, 1095
- Urrutia, T., Lacy, M., Spoon, H., et al. 2012, *ApJ*, 757, 125
- Vanden Berk, D. E., Richards, G. T., Bauer, A., et al. 2001, *AJ*, 122, 549
- Vestergaard, M. & Peterson, B. M. 2006, *ApJ*, 641, 689
- Véron-Cetty, M.-P., & Véron, P. 2006, *A&A*, 455, 773
- Virtanen, P., Gommers, R., Oliphant, T. E., et al. 2020, *Nature Methods*, 17, 261
- Webster, R. L., Francis, P. J., Peterson, B. A., Drinkwater, M. J., & Masci, F. J. 1995, *Nature*, 375, 469
- Weingartner, J. C. & Draine, B. T. 2001, *ApJ*, 548, 296
- Whiting, M. T., Webster, R. L., & Francis, P. J. 2001, *MNRAS*, 323, 718
- Wilkes, B. J., Schmidt, G. D., Cutri, R. M., et al. 2002, *ApJL*, 564, L65
- Woo, J.-H., Treu, T., Barth, A. J., et al. 2010, *ApJ*, 716, 269
- Wright, E. L., Eisenhardt, P. R. M., Mainzer, A. K., et al. 2010, *AJ*, 140, 1868
- Wu, J., Tsai, C.-W., Sayers, J., et al. 2012, *ApJ*, 756, 96
- Yip, C. W., Connolly, A. J., Szalay, A. S., et al. 2004, *AJ*, 128, 585
- Young, M., Elvis, M., & Risaliti, G. 2008, *ApJ*, 688, 128